Aerosol Science and Technology, 38:1206–1222, 2004

ISSN: 0278-6826 print / 1521-7388 online
DOI: 10.1080/027868290903916

Particle Morphology and Density Characterization by Combined Mobility and Aerodynamic Diameter Measurements. Part 2: Application to Combustion-Generated Soot Aerosols as a Function of Fuel Equivalence Ratio

Jay G. Slowik,[1] K. Stainken,[1] Paul Davidovits,[1] L. R. Williams,[2] J. T. Jayne,[2] C. E. Kolb,[2] Douglas R. Worsnop,[2] Y. Rudich,[3] Peter F. DeCarlo,[4] and Jose L. Jimenez[4]

[1]*Chemistry Department, Boston College, Chestnut Hill, Massachusetts, USA*
[2]*Center for Aerosol and Cloud Chemistry, Aerodyne Research Inc., Billerica, Massachusetts, USA*
[3]*Department of Environmental Sciences, Weizmann Institute, Rehovot, Israel*
[4]*Chemistry Department, CIRES, and Program in Atmospheric and Oceanic Sciences, University of Colorado at Boulder, Boulder, Colorado, USA*

Composition, shape factor, size, and fractal dimension of soot aerosol particles generated in a propane/O_2 flame were determined as a function of the fuel equivalence ratio (ϕ). Soot particles were first size-selected by a differential mobility analyzer (DMA) and then analyzed by an Aerodyne aerosol mass spectrometer (AMS). The DMA provides particles of known mobility diameter (d_m). The AMS quantitatively measures the mass spectrum of the nonrefractory components of the particles and also provides the vacuum aerodynamic diameter (d_{va}) corresponding to the particles of known mobility diameter. The measured d_m, d_{va}, and nonrefractory composition are used in a system of equations based on the formulation presented in the companion article to estimate the particle dynamic shape factor, total mass, and black carbon (BC) content. Fractal dimension was estimated based on the mass-mobility relationship. Two types of soot particles were observed depending on the fuel equivalence ratio. Type 1: for $\phi < 4$ (lower propane/O_2), d_{va} was nearly constant and independent of d_m. The value of d_{va} increased with increasing ϕ. Analysis of the governing equations showed that these particles were highly irregular (likely fractal aggregates), with a dynamic shape factor that increased with d_m and ϕ. The fractal dimension of these particles was approximately 1.7. These particles were composed mostly of BC, with the organic carbon content increasing as ϕ increased. At $\phi = 1.85$, the particles were about 90% BC, 5% PAH, and 5% aliphatic hydrocarbon (particle density = 1.80 g/cm^3). Type 2: for $\phi > 4$ (high propane/O_2), d_{va} was linearly proportional to d_m. Analysis of the governing equations showed that these particles were nearly spherical (likely compact aggregates), with a dynamic shape factor of 1.1 (versus 1 for a sphere) and a fractal dimension of 2.95 (3 for a sphere). These particles were composed of about 50% PAH, 45% BC, and 5% aliphatic hydrocarbons (particle density = 1.50 g/cm^3). These results help interpret some measurements obtained in recent field studies.

INTRODUCTION

In recent years, it has become apparent that climate change cannot be understood without accounting for the role played by tropospheric aerosols. These aerosols are known to be a complex mixture including mineral dust, inorganic salts, organic compounds, and soot. Of these, soot has been recently singled out as being of particular importance. Soot aerosols are generated during incomplete combustion of organic fuels such as coal, oil, and biomass. Field studies have shown that the percentage of carbonaceous material in tropospheric aerosols over the continental U.S. is 20–50% and is often higher than 50% in urban areas (Gray et al. 1986; Novakov and Penner 1993; Pandis et al. 1995; Cruz and Pandis 1997; Larson and Cass

Received 2 July 2004; accepted 29 October 2004.

We gratefully acknowledge Prof. Hai Wang of the University of Delaware for providing information on the soot formation process and Dr. James Allan for his work on AMS analysis software. Funding for this work was provided by the National Science Foundation Grants No. ATM-0212464 and CH-0089147, by the Department of Energy Grant No. DE-FG02-98ER62581, by the National Air and Space Administration Contracts No. NNH04CC09C and NNG04GA67G, and by the U.S.–Israel Binational Science Foundation Grant No. 1999134. J. Slowik is a recipient of a National Air and Space Administration Training Grant.

Address correspondence to P. Davidovits, Chemistry Department, Boston College, Merkert Center 223, 140 Commonwealth Avenue, Chestnut Hill, MA 02467, USA. E-mail: paul.davidovits.1@bc.edu

1989). Combustion-generated soot is often a significant part of these carbonaceous aerosols (Choi et al. 1993; McMurry et al. 2002). Recent field campaigns (Lelieveld et al. 2001; Koren et al. 2004) and modeling studies (Jacobson 2001; Ramanathan et al. 2001; Menon et al. 2002; Sato et al. 2003) have highlighted the role of soot aerosols in climate forcing.

Soot aerosols can affect climate by direct or indirect processes. In the direct process, soot aerosols alter the global radiation budget primarily by absorbing light and also by scattering light. This reduces the net solar radiative flux to the earth's surface. Light absorption warms the atmosphere in the vicinity of the aerosols. Likewise, deposition of soot on polar ice increases the absorption of solar energy, causing increased heating of the ice. Such heating has been suggested to be a major cause of the rapid melting of glaciers, sea ice, and permafrost (Hansen and Nazarenko 2004).

The indirect effects of soot aerosols on climate are due to the ability of soot particles to alter cloud properties by serving as cloud condensation nuclei (CCN; Ramanathan et al. 2001; Menon et al. 2002). The CCN ability of aerosols depends on their size and chemical composition. For clouds with the same liquid water content, an increase in the number of CCN in a cloud leads to smaller cloud droplets. These clouds are expected to be more reflective, have a longer lifetime, and produce less precipitation (Twomey et al. 1984; Albrecht 1989).

The carbonaceous material in soot particles can be divided into two categories: relatively volatile organic carbon (OC) and a nonvolatile fraction commonly called black carbon (BC) as described later. The OC component of soot consists primarily of polycyclic aromatic hydrocarbons (PAH) and aliphatic hydrocarbons (AL). The BC component is primarily graphitic carbon, although the exact composition is not well known. The BC component makes soot the strongest light absorber among atmospheric aerosols. BC has been proposed as the second-most important contributor to global warming, following CO_2 (Jacobson 2001).

Freshly generated soot particles are initially hydrophobic and are unlikely to act as CCN. With age, soot particles may acquire coatings such as acids, salts, and organics. Field studies indicate that soot is found in 10–45% of sulfate particles and seldom exists in pure form in the atmosphere (Posfai et al. 1999). Further, the soot surface may become partially oxidized by interactions with gas-phase radicals. The sulfate coatings and partial oxidation products may make the soot hydrophilic. An understanding of the soot aging process and its effect on particle hygroscopicity is necessary to address the potential of soot as a CCN.

Soot generation by combustion is a complex process, and there is a large body of literature on the subject (see, for example, Haynes and Wagner 1981; Smith 1981; Frenklach et al. 1984; Bockhorn 1994). However, the characteristics of the soot are remarkably unaffected by the type of fuel burned. This is because all hydrocarbon fuels tend to follow similar combustion mechanisms. The fuel first undergoes pyrolysis, a process of thermal degradation and cracking of complex fuel molecules, which produces low molecular weight radicals. PAHs are formed subsequently by a series of radical reactions with soot precursors such as acetylene radicals. Further reactions with small precursor molecules result in the growth of the PAH structures until they become large enough to serve as particle nuclei. The high temperature of the flame causes most of the hydrogens to be stripped away, leaving small spherules with a high carbon-to-hydrogen ratio. These spherules form the primary component of BC, the refractory component of soot. (In this study, refractory refers to components that do not vaporize below about 550°C under high vacuum, which are the conditions at the aerosol mass spectrometer (AMS) detector.) These spherules may coagulate, forming aggregate particles. Electron microscopy studies show that the BC spheres are typically about 15–30 nm in diameter, depending on the flame conditions (Palmer and Cullis 1965; Heywood 1988). As the flame cools, hydrocarbon species such as PAHs and aliphatics may adsorb on the agglomerate surfaces (Glassman 1996).

Detailed soot characteristics are highly dependent on flame temperature and the fuel equivalence ratio (ϕ), which control the concentration of soot precursors, the extent of dehydrogenation, and the amount and type of adsorbed hydrocarbons. The equivalence ratio is defined as

$$\phi = \frac{(\text{Molecules of Fuel/Molecules of } O_2)_{\text{actual}}}{(\text{Molecules of Fuel/Molecules of } O_2)_{\text{stoichiometric}}} \quad [1]$$

The stoichiometric ratio is the one required for complete combustion of the fuel to CO_2 and H_2O. In this study, where propane is used as fuel, the stoichiometric ratio is 0.2. The flame temperature is linked to the equivalence ratio if all the physical parameters of the flame environment are fixed, as is the case in this study. In the present studies, where the flame is overall fuel-rich, the flame temperature is inversely related to ϕ. Flame temperature has been shown to affect the onset of sooting and soot aerosol number density (Milliken 1962; Schug et al. 1980).

The role played by soot aerosols in climate is likely to be determined by the optical and hygroscopic properties of the aerosols. These properties depend principally on particle composition, shape, and size, which in turn are determined mainly by the combustion conditions that generate the soot and on the subsequent transformations of the particles in the atmosphere. Here we present results of studies measuring the effect of the fuel equivalence ratio on the physical morphology and composition of soot particles. The particle properties are determined using the theoretical framework developed in the companion article (DeCarlo et al. 2004).

EXPERIMENTAL TECHNIQUE

Apparatus

A schematic diagram of the apparatus used in this study is shown in Figure 1. The data obtained from this apparatus can be used to estimate the size, dynamic shape factor,

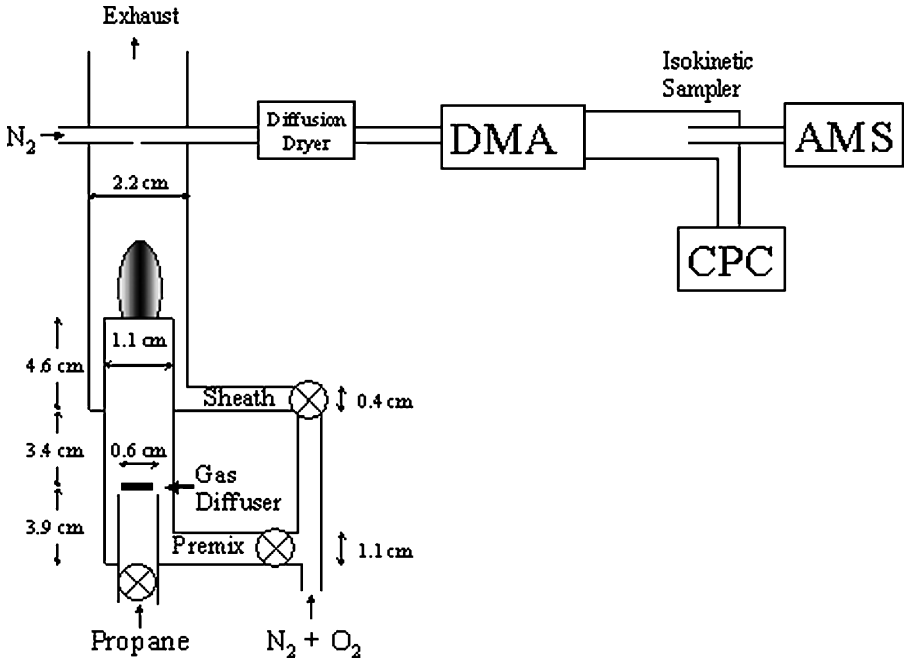

Figure 1. Apparatus for soot production and analysis (note diagram is not to scale).

density, chemical composition, and fractal dimension of the particles.

Soot particles are generated by the combustion of gaseous fuel (propane in the present studies; 99.0%, AGA Gas, Billerica, MA, USA) premixed with a mixture of N_2 and O_2 (99.0%, AGA Gas) The dimensions of the burner are shown in Figure 1. The propane flow varies from 90 to 170 cm^3/min. The premixed N_2/O_2 flow varies from 500 to 1100 cm^3/min and is always about 30% O_2. In the present experiments, a visual inspection shows that this N_2/O_2 ratio resulted in a consistently stable flame and smoke plume. The propane and N_2/O_2 are mixed by a gas diffuser. The diffuser is a small plug at the end of the propane gas line that directs the flow away from the center line of the tube, facilitating mixing.

The flame is surrounded by a second N_2/O_2 flow ($\sim$2 l/min), called the "sheath" flow, that isolates the flame from the walls of the Pyrex tube in which the burner is mounted. The particles are sampled approximately 25 cm above the base of the flame through a 2 mm pinhole into a laminar flow of N_2 (0.5–1.0 l/min), which together with the sample flow from the flame produces a total flow of 1.1 l/min. The pinhole is approximately 2.5–3 times the height of the luminous flame, depending on flame conditions. Soot particles are drawn into the N_2 flow by the pressure drop across the pinhole resulting from the difference in flowrate between the N_2 flow and total flow. The flame burns at a pressure of approximately 1 atm. The pinhole can be translated along the diameter of the tube carrying the products of the flame. However, in this study the sampling was performed approximately on the center line of the flame for all flame conditions.

The aerosol flow is dried in a diffusion dryer containing anhydrous calcium sulfate (Drierite, Aldrich, Milwaukee, WI, USA) and size-selected by a differential mobility analyzer (DMA; TSI Inc., Model 3071A, St. Paul, MN, USA). This size selection is based on the drift velocity of charged aerosols in an electric field (Hinds 1999). Thus the DMA selects particles of known mobility diameter (d_m)[1]. In the present study the particles selected by the DMA range from approximately 100–400 nm in mobility diameter. The DMA setting determines the particle d_m to about $\pm$10% (Flagan 1999).

After the aerosol flow exits the DMA it is split into two branches. Of the total flow, 0.1 l/min is sampled by a calibrated Aerodyne AMS and 1.0 l/min is directed to a condensation particle counter (CPC) that measures particle number density. In the present experiments the number density was in the range of 100–15,000 particles/cm^3, depending on experimental conditions such as equivalence ratio, particle size, and dilution flows. Sampling at the AMS/CPC junction is isokinetic to avoid distortion of the size distribution or number density. The AMS flow is taken from the center line of the initial flow.

Particles enter the AMS through a 100 μm orifice and pass through an aerodynamic focusing lens (Liu et al. 1995a, b; Jayne et al. 2000; Zhang et al. 2002, 2004a). Here the particles are focused into a narrow beam, typically 100 μm wide at the exit of

[1]Mobility diameter (d_m) is the diameter of a sphere that has the same drift velocity in an electric field as the particle under study. The mobility diameter depends on particle size and shape. See the companion article (DeCarlo et al. 2004) and section "Definitions of Mobility and Vacuum Aerodynamic Diameters" below for a more detailed treatment.

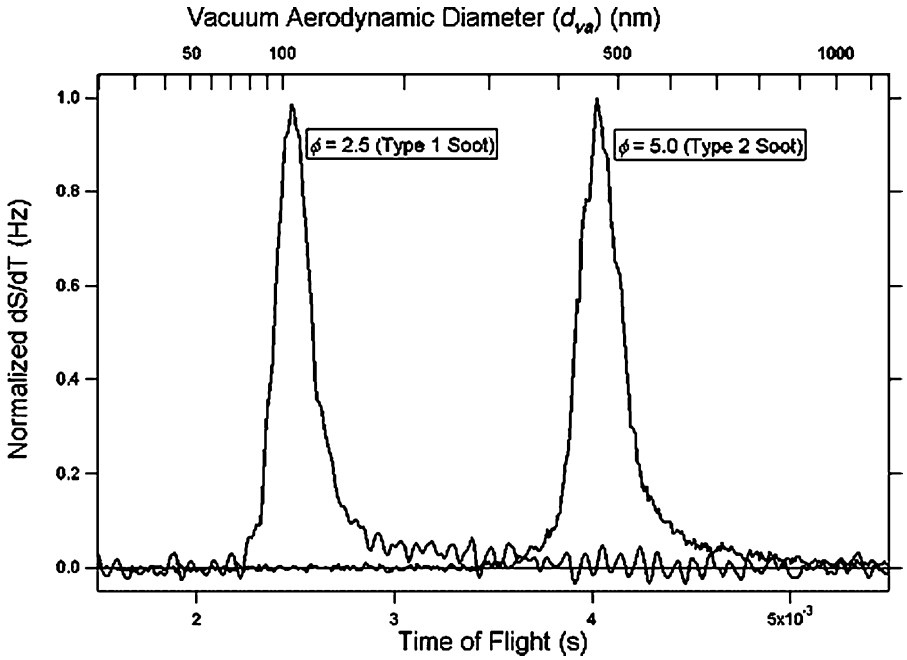

Figure 2. Time-of-flight mass distribution for soot (d_m = 350 nm, ϕ = 2.5 and 5.0, m/z 226, particle number density ~ 5000 particles/cc). Note the abscissa does not start at t = 0, and the arrival time in this case is 4.0 ms. (The meaning of the two types of soot is discussed in section "Results.")

the lens (Heberlein et al. 2001). In the process of exiting the lens, the particles are accelerated into a high vacuum chamber. The final velocity of the particles is inversely related to their vacuum aerodynamic diameter (d_{va}).[2] The aerodynamic lens used in this experiment efficiently focuses particles with vacuum aerodynamic diameter in the range of 60–600 nm.

Upon exiting the aerodynamic lens, pulses of particles are formed by a spinning chopper wheel (110 Hz). The particle pulses pass through a high vacuum chamber (2×10^{-7} torr) and impact upon a resistively heated surface (T ~550°C) at the end of the chamber, where the nonrefractory component of the aerosol is thermally vaporized. At this point the particle beam has diverged and is typically about 2 mm in diameter at the vaporizer for the soot aerosols analyzed in this study.

The vaporized molecules are ionized by electron impact (45 eV in this study) and detected by a quadrupole mass spectrometer (Balzers QMA 410). The vacuum aerodynamic diameter is determined from the particle time-of-flight between the chopper and the vaporizer (Jayne et al. 2000). In the present experiments, the time of flight is in the range 2.5 ms for d_{va} = 100 nm to 4.0 ms for d_{va} = 400 nm.

[2]Vacuum aerodynamic diameter is the diameter of a solid spherical particle of unit density that has the same aerodynamic properties in the free-molecular regime as the particle under study (Jayne et al. 2000; Jimenez et al. 2003b, c). The vacuum aerodynamic diameter depends on particle size, density, and shape. See the companion article (DeCarlo et al. 2004) and section "Definitions of Mobility and Vacuum Aerodynamic Diameters" below for a more detailed treatment.

Signal Detection

The AMS alternates between two modes of operation (Jimenez et al. 2003a). In the first mode, the entire m/z (ratio of ion mass to charge) range of the quadrupole mass spectrometer is scanned and the chopper is moved so that the particle beam is alternately completely blocked and completely open. This yields a complete mass spectrum for the particle (and gas) ensemble. The ion intensities (after background subtraction) can be quantitatively converted to a particle mass/volume of air impinging on the vaporizer (Allan et al. 2003a). In the second mode, the quadrupole mass filter is set to specific m/z values characteristic of the particle being studied. Particle time-of-flight data are recorded. This mode yields vacuum aerodynamic diameter size distributions of the particles containing the specific m/z fragments detected by the mass filter. The duration of each mode of operation is computer-controlled and is typically set at 20 s.

In the time-of-flight mode, the signal pulse resulting from the vaporization of a single soot particle has a sharp rising edge of about 20 μs and is about 60 μs in width. For a given vaporizer temperature, this width is determined by the vaporization time, which depends on particle size and composition. The ion signals from individual particles are accumulated and averaged.

In Figure 2 we show two such averaged signals. Here the soot particles were size selected at d_m = 350 nm for equivalence ratios (ϕ) of 2.5 and 5.0. Ion signals were monitored at m/z = 226. A particle number density of 5000 particles/cm^3 was measured by the CPC. The signal in Figure 2 is an average of about 3600 particles/s impinging on the vaporizer and collected

in about 15 s. The signal here is about 250 μs wide. This width is determined by the width and speed of the chopper slit, by the particle vaporization time, and by the DMA transfer function. The particle arrival time at the heater is taken to be the peak of the distribution shown in Figure 2.

Calibration

To determine quantitatively the mass composition of the soot particles, the AMS has to be calibrated for particle collection efficiency and vaporized plume ionization efficiency. To calibrate ionization efficiency, 350 nm NH_4NO_3 particles were sampled by the AMS. NH_4NO_3 is used as a standard because it is known to vaporize completely in the AMS, and the number of particles detected by the AMS is quantitatively the same as recorded by the CPC (Jayne et al. 2000). Single-particle vaporization events were monitored, and the number of ions detected by the AMS in each event was measured, yielding the ionization efficiency for nitrate (number of nitrate ions detected per vaporized NH_4NO_3 molecule $\sim 8 \times 10^{-7}$). The ionization efficiency for other molecules is approximately proportional to their molecular weight with a correction factor that varies with the chemical nature of the molecule (Jimenez et al. 2003a). Thus, the NH_4NO_3 calibration has to be scaled in order to be applicable for aliphatic hydrocarbons and PAHs. For the organic species the NO_3 ionization efficiency is multiplied by a relative ionization efficiency (RIE) representative of the molecule(s) under study. A factor of RIE = 1.4 for aliphatic hydrocarbons was determined by comparing NH_4NO_3 quadrupole signals to those obtained with known sized decane and lubricating oil aerosols. For PAHs, the relative ionization efficiency was determined to be 1.35 using pyrene as a surrogate for all PAHs.

The collection efficiency of the AMS is determined by how well the particles are focused by the aerodynamic lens. If the particle beam is too wide, some particles will miss the vaporizer. Particle shape plays a role in focusing due to lift forces on irregular particles. Spherical particles generally focus into a smaller beam than nonspherical particles (Liu et al. 1995b; Jayne et al. 2000; Kane and Johnston 2000; Tobias et al. 2000).

The size of the focused particle beam is measured by a thin wire ($\sim$1.0 mm) that is translated across the particle beam by a computer-controlled stepper motor. The signal attenuation as a function of the wire position yields the beam shape and collection efficiency (as calculated assuming a 2D circular Gaussian beam shape; Huffman et al. in preparation). Collection efficiency was estimated to be between about 90 and 95%, depending on the type of soot generated in the flame. Knowledge of both the ionization and collection efficiencies permits the quantitative determination of the nonrefractory mass in the particles (see Jayne et al. 2000). Because the aerosols are vaporized at a relatively low temperature (about 550°C), the AMS does not directly detect the BC content of the soot. However, the BC content of the soot can be estimated by mass balance.

DATA ANALYSES

In both the DMA and AMS instruments the aerosol particles reach final velocities, and these velocities are the measured quantities that yield the particle equivalent diameters provided by the instruments. The DMA provides the mobility diameter (d_m) and the AMS provides the vacuum aerodynamic diameter (d_{va}). The AMS and CPC measurements together yield the vaporizable OC mass per particle entering the AMS. As is shown in the following section, further data analyses allow the estimate of particle density, composition, dynamic shape factor, and fractal dimension of the soot particles. This additional information is obtained from the functional relationships between the mobility and vacuum aerodynamic diameters described in the companion article (DeCarlo et al. 2004) and summarized in the next section.

Definitions of Mobility and Vacuum Aerodynamic Diameters

In the DMA, charged aerosol particles are accelerated in an electric field. Terminal velocity (V_{TE}) is attained when the electric and drag forces are balanced. The DMA terminal velocity yields the particle mobility diameter, d_m, which can be expressed in terms of the volume equivalent diameter (d_{ve}) and the particle shape (expressed via the dynamic shape factor (χ)). The definitions of these parameters are given in the companion article (DeCarlo et al. 2004) and are summarized briefly here for completeness. The volume equivalent diameter (d_{ve}) is defined as the diameter of a sphere with the same volume as the particle, that is (Hinds 1999; Baron and Willeke 2001),

$$d_{ve} = \left(\frac{6}{\pi} \cdot \text{Volume} \right)^{1/3}. \quad [2]$$

The dynamic shape factor (χ) accounts for the effect of nonspherical shape on the particle drag force and is defined in terms of d_{ve} as (Hinds 1999; Baron and Willeke 2001)

$$\chi \equiv \frac{F_D}{3\pi \eta V d_{ve}}. \quad [3]$$

Here F_D is the drag force on the particle. The denominator in Equation (3) is the drag on the volume equivalent sphere (a sphere with diameter d_{ve}), where η is the gas viscosity and V is the velocity of the particle. For a spherical particle, $\chi = 1$.

As shown in the companion article (DeCarlo et al. 2004), the mobility diameter can be related to d_{ve} by

$$d_m = \frac{d_{ve} C_c(d_m) \chi_t}{C_c(d_{ve})}. \quad [4]$$

Here C_c is the Cunningham slip correction factor, which is introduced to account for the reduced drag on particles with a diameter on the order of or smaller than the gas mean free path λ. The dynamic shape factor is known to vary with flow regime. In the DMA, the particles are in the transition regime, and we denote the dynamic shape factor as χ_t (DeCarlo et al. 2004). The

Cunningham slip correction factor is a function of the aerosol diameter and the molecular mean free path. Diameter has a well-defined meaning only for a spherical particle. For nonspherical particles it is convenient to define an equivalent diameter, here denoted d'. We have already introduced three such diameters (d_{ve}, d_m, d_{va}) in this discussion. Here we express the Cunningham factor in terms of d' as formulated empirically by Allen and Raabe (1982, 1985) as

$$C_c(d') = 1 + \frac{\lambda}{d'}\left(2.34 + 1.05e^{-0.39d'/\lambda}\right). \quad [5]$$

The vacuum aerodynamic diameter, d_{va}, is determined from the measured time of flight of the particle from the chopper wheel (after the lens) to the vaporizer. The time of flight depends on the final velocity of the particle attained at the exit from the aerodynamic lens (the acceleration of the particle in the lens is due to the pressure drop between the lens entrance (2 torr) and exit (10^{-4} torr)). This final velocity has been experimentally related to d_{va} (Jayne et al. 2000; Bahreini et al. 2003).

As shown in the companion article (DeCarlo et al. 2004) and by Jimenez et al. (2003b, c), d_{va} may be formulated in terms of the particle dynamic shape factor in the free-molecular regime (χ_v), the volume equivalent diameter (d_{ve}), and the particle density (ρ_p) as

$$d_{va} = d_{ve} \cdot \frac{\rho_p}{\rho_0} \cdot \frac{1}{\chi_v}. \quad [6]$$

Here ρ_o is the unit density (1 g/cm^3). For a spherical particle with unit material density and no internal voids, $d_{va} = d_{ve}$. Note that the particle density (ρ_p), equals the material density (ρ_m) only in the absence of internal voids, as described in detail by DeCarlo et al. (2004).

As is evident from the definition of d_{ve} (Equation (2)), the total particle mass (m_p) can be expressed as (DeCarlo et al. 2004)

$$m_p = \frac{\pi}{6} d_{ve}^3 \rho_p. \quad [7]$$

The particles are now described by a system of Equations (4), (6), and (7), relating the 7 parameters of interest, namely d_m, d_{va}, d_{ve}, χ_t, χ_c, m_p, and ρ_p. The mobility diameter and the vacuum aerodynamic diameter are determined experimentally, leaving 5 unknowns (d_{ve}, χ_t, χ_c, m_p, and ρ_p). Clearly the system of equations is underdetermined. However, in our experiments the mass per particle of the nonrefractory component is also measured. As is shown in the next section, this additional measurement and some reasonable assumptions allow us to estimate the unknown parameters needed to solve the equations.

Estimate of Particle Mass, Density, and Dynamic Shape Factor

One possible approximation to reduce the underdetermination of the system of equations is to assume $\chi = \chi_t = \chi_v$. The limitations of this approximation are explored in the companion article (DeCarlo et al. 2004). With this approximation, the system is reduced to 3 equations and 4 unknowns.

Further, we assume that the soot particles are composed of an OC component (PAH and aliphatic) that is measured by the AMS, and a BC component that the AMS does not detect because the BC fraction does not vaporize at 550°C. The particle mass (m_p) can then be expressed as

$$m_p = m_{\mathrm{BC}} + m_{\mathrm{PAH}} + m_{\mathrm{AL}}. \quad [8]$$

Here m_{BC}, m_{PAH}, and m_{AL} are the mass per particle of the black carbon, PAH, and aliphatic components, respectively.

If we assume that the soot particles have no internal voids, the overall particle density (ρ_p) is

$$\rho_p = \frac{m_{\mathrm{BC}} + m_{\mathrm{PAH}} + m_{\mathrm{AL}}}{V_p} \quad [9]$$

Here V_p is the particle volume (by definition based on d_{ve}). Note that V_p and ρ_p are equal to the material volume and density, respectively, due to the assumption of no internal voids (see DeCarlo et al. 2004 for a more detailed discussion). Finally, by assuming that the 3 phases (BC, PAH, and aliphatics) are immiscible, we can write Equation (9) as

$$\rho_p = \frac{m_{\mathrm{BC}} + m_{\mathrm{PAH}} + m_{\mathrm{AL}}}{\frac{m_{\mathrm{BC}}}{\rho_{\mathrm{BC}}} + \frac{m_{\mathrm{PAH}}}{\rho_{\mathrm{PAH}}} + \frac{m_{\mathrm{AL}}}{\rho_{\mathrm{AL}}}}. \quad [10]$$

Here ρ_{BC}, ρ_{PAH}, and ρ_{AL} are the material densities of BC, PAH, and aliphatics, respectively. We can make the following reasonable estimates for these densities. The density of BC (ρ_{BC}) is in the range of ~1.8–2.1 g/cm^3 (Lide 1992). In this study we assume $\rho_{\mathrm{BC}} = 2.0$ g/cm^3. The density of aliphatic hydrocarbons (ρ_{AL}) is estimated at 0.85 g/cm^3 based on the densities of long straight-chain aliphatics and lubricating oil. For PAHs, the average molecular weight of the mass spectrum was calculated, and the density of the PAH with that molecular weight was chosen. The density of PAHs (ρ_{PAH}) is estimated to be 1.3 g/cm^3, which is approximately the density of pyrene.

Equation (6) can be rewritten (using Equation (10)) as

$$d_{va} = \frac{d_{ve}}{\chi \rho_0}\left(\frac{m_{\mathrm{BC}} + m_{\mathrm{PAH}} + m_{\mathrm{AL}}}{\frac{m_{\mathrm{BC}}}{\rho_{\mathrm{BC}}} + \frac{m_{\mathrm{PAH}}}{\rho_{\mathrm{PAH}}} + \frac{m_{\mathrm{AL}}}{\rho_{\mathrm{AL}}}}\right) \quad [11]$$

Further, Equation (7) can be rewritten (using Equations (8) and (10)) as

$$\frac{m_{\mathrm{BC}}}{\rho_{\mathrm{BC}}} + \frac{m_{\mathrm{PAH}}}{\rho_{\mathrm{PAH}}} + \frac{m_{\mathrm{AL}}}{\rho_{\mathrm{AL}}} = \frac{\pi}{6} \cdot d_{ve}^3. \quad [12]$$

To summarize, we have now expressed the particle properties in terms of Equations (4), (11), and (12), the three unknowns d_{ve}, χ, and m_{BC}, and the measured quantities d_{va}, d_m, m_{PAH}, and m_{AL}. This system of equations can now be solved iteratively to yield

d_{ve}, χ, m_{BC}, ρ_p, and m_p. However, as is discussed in the next section, the relationship between d_{va} and d_m is such that m_p can be estimated within about 10% even under conditions where the density and composition are not known.

Further Comments on Estimating Particle Mass

It is interesting to note that in some cases the full set of relations developed in the previous section may not be needed to obtain the mass of the particle. Simply a measurement of d_{va} and d_m may provide a sufficiently accurate particle mass determination. In the companion article, DeCarlo et al. (2004) propose an expression for estimating particle mass solely from measurements of d_{va} and d_m. These two parameters are used to estimate an effective particle density (ρ_{eff}). The estimate of ρ_{eff} is then used with d_m to calculate particle mass (i.e., $m_p = \frac{\pi}{6} d_m^3 \rho_{eff}$). As stated by DeCarlo et al. (2004), this expression systematically overpredicts particle mass and yields a value that is within about a factor of 2 of the actual particle mass.

By definition, $m_p = (\pi/6) \cdot d_{ve}^3 \cdot \rho_p$ (see Equation (7)), and in terms of this expression $dm_p/m_p = d\rho_p/\rho_p$. However, when d_{va} and d_m are measured (as they are in these experiments) and ρ_p is estimated, then the combination yields a value of m_p that is significantly less sensitive to the uncertainty in ρ_p. That is, $dm_p/m_p < d\rho_p/\rho_p$. For example, if the density of a typical soot particle with $d_m = 200$ nm and $d_{va} = 260$ nm is known to within about 40% of 1.5 g/cm^3 (a typical range of component densities in soot), d_{va} and d_m yield the particle mass to an accuracy of about 7%. The reduced dependence of dm_p/m_p on $d\rho_p/\rho_p$ is derived in Appendix B.

The starting point for the derivation in Appendix 2 is the following relationship obtained from Equations (4) and (6):

$$\frac{\rho_p \cdot d_{ve}^2}{C_c(d_{ve})} = \frac{d_m \cdot d_{va} \cdot \rho_o}{C_c(d_m)}. \quad [13]$$

This relationship requires the assumption that $\chi = \chi_t = \chi_v$. As shown in Appendix B, between the limit of small and large values of d_{ve} the dependence of dm_p/m_p on $d\rho_p/\rho_p$ increases from 0 to $1/2$. In other words, mass estimation by the measurement of d_m and d_{va} without a precise knowledge of ρ_p is more accurate for smaller particles. Between these two limiting cases, the relationship between dm_p/m_p and $d\rho_p/\rho_p$ is obtained by a numerical solution to Equation (13). The method of calculation and some results are shown in Appendix B.

Fractal Dimension of Soot

As described in the companion article, with some additional assumptions we can estimate the fractal dimension (D_f) of the soot particles. Scanning electron microscopy data from other studies show that soot aerosols are agglomerates of BC spherules with a diameter of about 15–30 nm coated with organic compounds (Heywood 1988). The fractal dimension is formulated (Hinds 1999) as

$$N_{pp} = C\left(\frac{2R_g}{d_{pp}}\right)^{D_f}. \quad [14]$$

Here N_{pp} is the number of primary particles (i.e., BC spherules) in the agglomerate, R_g is the radius of gyration, and d_{pp} is the diameter of the primary particles. The parameter C is a constant for particles of the same fractal character.

It has been shown that under some conditions R_g is linearly proportional to the mobility diameter under some conditions (that is, $k_1 d_m = R_g$, where k_1 is the proportionality constant). This relationship has been shown to hold for all particles in the continuum regime, and for particles with $D_f \geq 2$ in any flow regime (Schmidt-Ott et al. 1990; DeCarlo et al. 2004; Van Gulijk et al. 2004). However, it is uncertain how far into the transition regime this relationship holds for particles with $D_f \leq 2$. In this study, the particles are in the transition regime. Nevertheless, in order to proceed we assume that R_g and d_m are proportional to each other. This assumption introduces some additional uncertainty into our measurements, as discussed in section "Fractal Dimension" below.

Further, we assume that d_{pp} is constant for a given equivalence ratio and independent of the overall size of the soot agglomerate. Since the soot particle is an agglomerate of primary particles, we assume that N_{pp} is linearly proportional to the BC mass (m_p) of the agglomerate. Equation (14) can then be rewritten as

$$m_p = C' \cdot d_m^{D_f}. \quad [15]$$

This expression is known as the mass-mobility relationship (Park et al. 2003). The fractal dimension is obtained from Equation (15) as the slope of $\log(m_p)$ versus $\log(d_m)$. The fractal dimension is 3 for a sphere. This is evident because for a sphere mass (m_p) is proportional to d_m^3 (for a sphere, $d_m = d_{ve}$). The fractal dimension decreases for less regular particles to a minimum value of 1 for an infinitely long linear aggregate. The intercept of such a log-log plot is $\log(C')$. However, the parameters defining C' are not known, and therefore we do not obtain significant information from the intercept.

RESULTS

Experiments were conducted to determine the dependence of the morphology and composition of soot particles on the equivalence ratio of a premixed propane flame. Studies were conducted at equivalence ratios (ϕ) ranging from 1.85 to 6.25. At an equivalence ratio below ~1.85, soot particles were no longer produced in detectable quantities. This is in good agreement with the expected sooting limit of ~1.75 (Hai Wang, private communication). As was stated earlier, all sampling was performed on the center line of the flame. Particles of known (i.e., preselected) mobility diameter (d_m) enter the AMS. Here the vacuum aerodynamic diameter d_{va} and the corresponding mass spectrum of the vaporized organics contained in the soot are quantitatively determined.

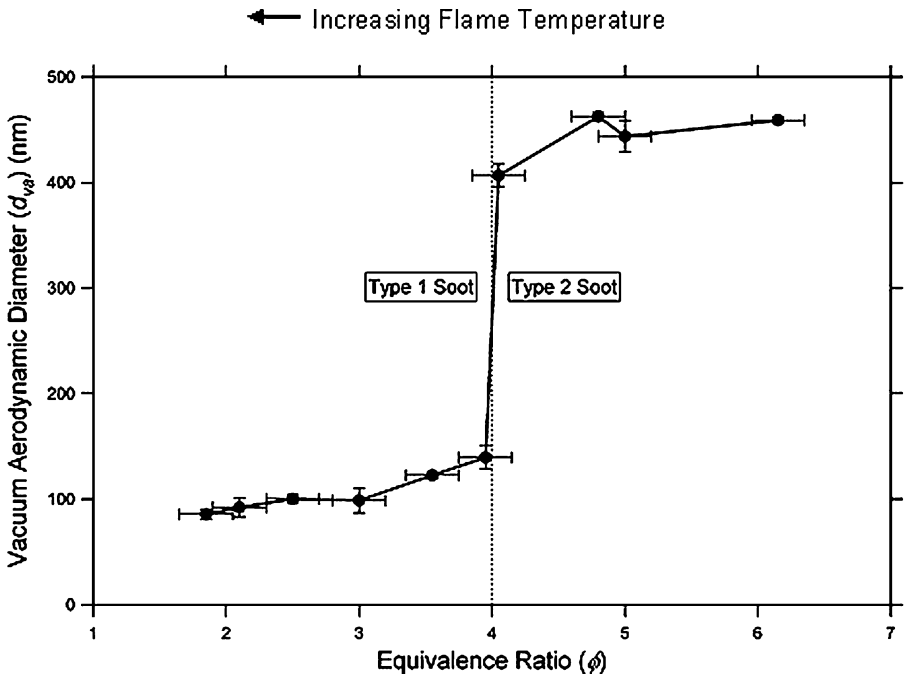

Figure 3. Vacuum aerodynamic diameter of $d_m = 350$ nm soot as a function of equivalence ratio. There is a sharp boundary between type 1 and type 2 soot, occurring at a equivalence ratio of about 4.0.

Observed Relationship between Vacuum Aerodynamic Diameter and Mobility Diameter

As shown in Figures 3 and 4, two distinct types of soot were observed depending on the equivalence ratio (ϕ). The sharp transition between these two types of soot, at $\phi \sim 4.0$, is shown in Figure 3, which is a plot of d_{va} versus ϕ for soot particles with $d_m = 350$ nm. For convenience of discussion we will designate the soot produced at lower ϕ as type 1 and at ϕ as type 2. For type 1 soot, d_{va} increases from 85 to 140 nm as ϕ increases from 1.85 to 4.0. The increase in d_{va} for constant d_m as ϕ increases is

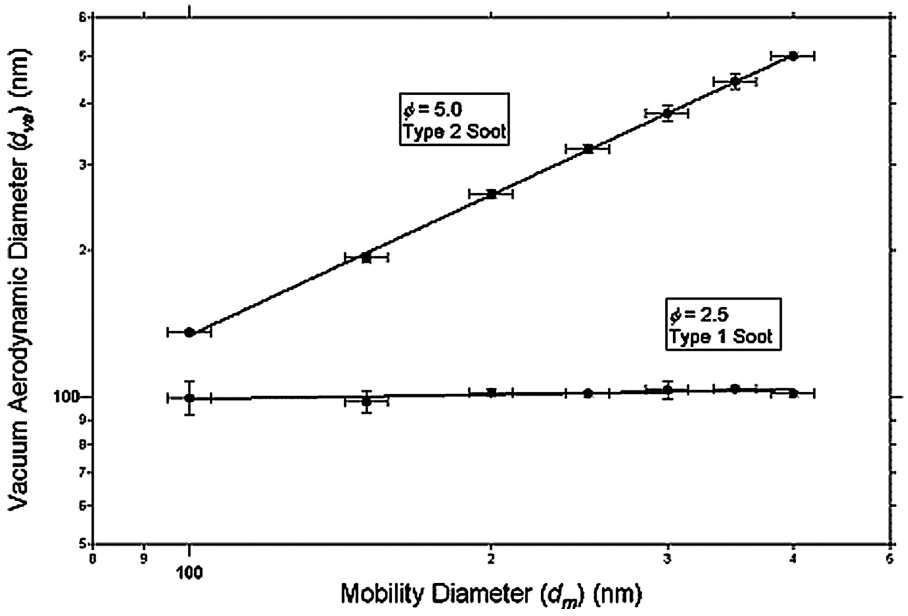

Figure 4. Vacuum aerodynamic diameter versus mobility diameter for two equivalence ratios. For $\phi = 2.5$ (type 1 soot), $d_{va} \sim 102$ nm regardless of d_m. For $\phi = 5.0$ (type 2 soot), $d_{va} = 1.3 \times d_m$.

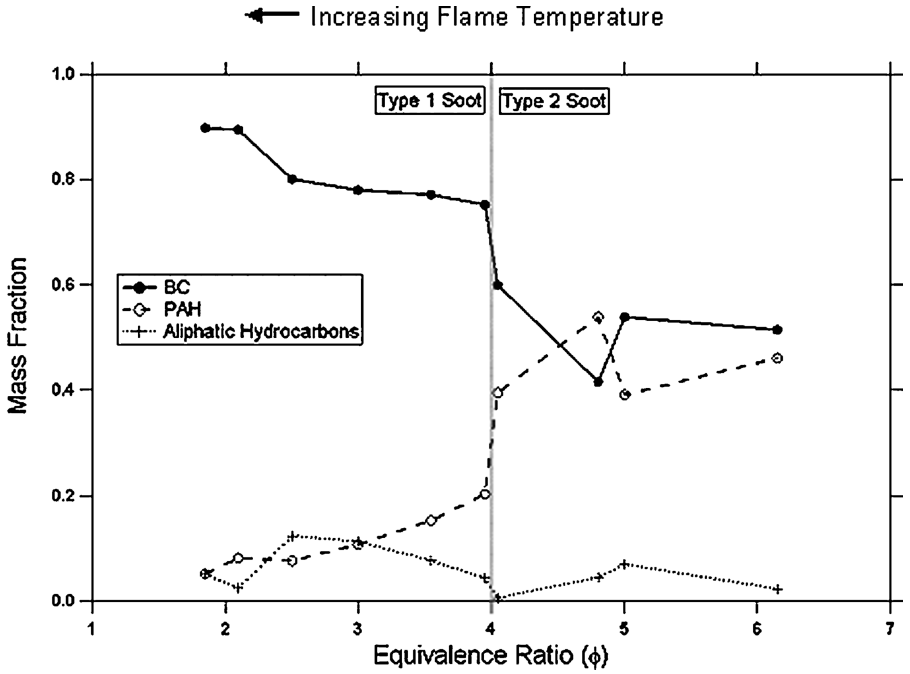

Figure 5. Fractional mass composition of the soot particles as a function of equivalence ratio. Particle component mass fractions are independent of d_m.

quantitatively the same for all type 1 soot studied here in the mobility diameter range $d_m = 100$–400 nm. On the other hand, for type 2 soot d_{va}/d_m remains constant at about 1.3 (455 nm/350 nm) as ϕ increases from 4.0 to 6.25. (This constancy in the d_{va}/d_m ratio is also evident in our results shown in Figures 5–7).

At a given ϕ, the relationship of d_{va} and d_m is different for the two types of soot. The difference is shown in Figure 4, which is

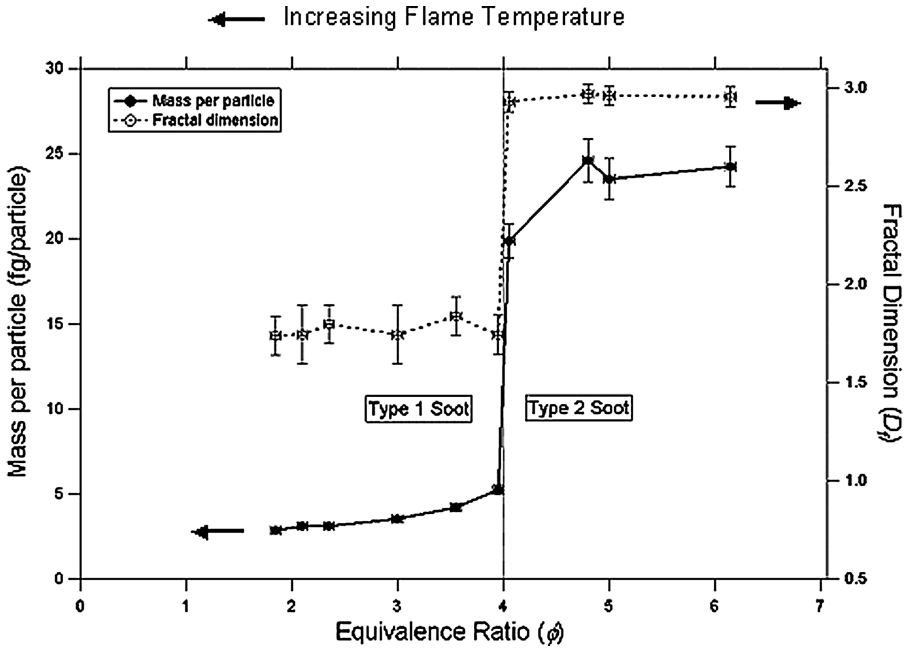

Figure 6. Particle mass and fractal dimension as a function of equivalence ratio. Mass per particle is shown for soot particles with mobility diameter = 350 nm. Fractal dimension is independent of mobility diameter.

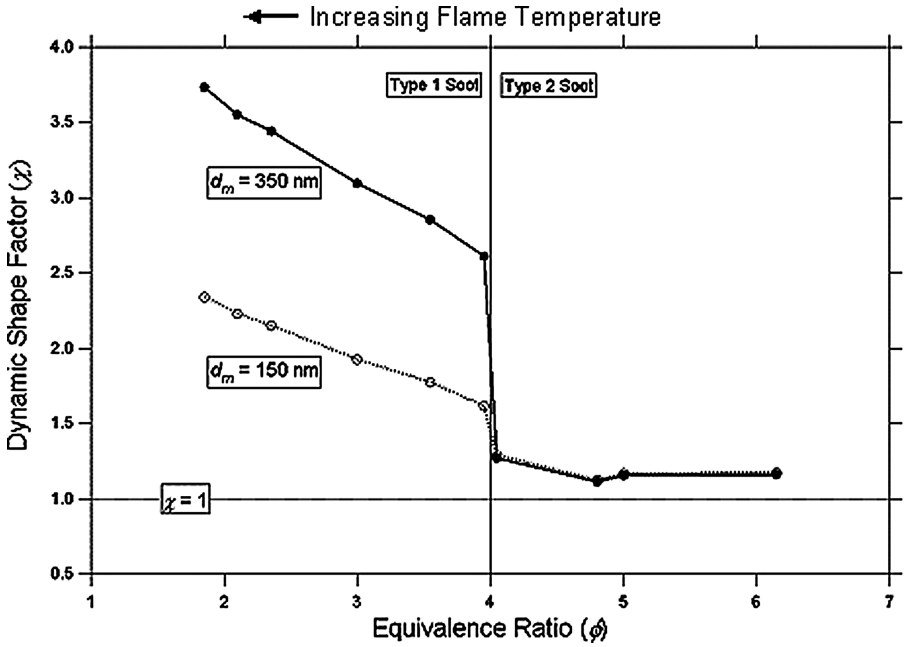

Figure 7. Dynamic shape factors for soot (estimated with the assumption $\chi = \chi_t = \chi_v$). For Type 1 soot, χ ranges from about 1.5 to 3.5 over the size range studied. For Type 2 soot, $\chi = 1.1$. $\chi = 1$ for a sphere.

a plot of d_{va} versus d_m for $\phi = 2.5$ and 5.0, where d_{va} is determined from the time-of-flight mass distributions as described in section "Signal Detection" below. For $\phi < 4.0 \pm 0.2$, the vacuum aerodynamic diameter is nearly a constant and independent of d_m for the range of mobility diameters in this study. On the other hand, for $\phi > 4.0 \pm 0.2$, the mobility diameter is linearly proportional to the vacuum aerodynamic diameter. Specifically, $d_{va} = 1.3 \times d_m$ (as is also shown in Figure 3).

Chemical Composition: Organic Carbon

Another difference between these two types of soot is their chemical composition. In Figure 8 we show the mass spectrum of the OC component (i.e., the nonrefractory fraction) for the two types of soot. The data in Figure 5 were obtained for soot of $d_m = 350$ nm and equivalence ratios (ϕ) of 2.5 (type 1 soot) and 5.0 (type 2 soot). The OC component of type 1 soot consists of comparable amounts of PAHs and aliphatic hydrocarbons. However, PAH species account for most of the OC in type 2 soot, although aliphatic hydrocarbons are present in small amounts (note that the mass peaks below about m/z 175 are doubly ionized PAHs, not aliphatic hydrocarbons). The y axes are the absolute mass per particle in femtograms (fg) (1 fg $= 10^{-15}$ g) and show that the total amount of OC is greater in type 2 than in type 1 soot. Note that no correction for partial ion transmission at large m/z or changes in the relative response of the electron multiplier detector versus m/z has been made. The mass spectrum in Figure 8 shows the presence of a wide range of PAH compounds, and is consistent with the presence of molecules such as anthracene, pyrene, benzopyrene, and coronene. The OC composition of soot is similar over the full range of d_m studied (100–400 nm) for both types of soot. Similar PAH distributions have been observed in some field studies (Jose Jimenez, private communication). However, the PAH distribution observed in this study is different from some distributions observed from sampling within the flame (Dobbins et al. 1998). These authors observed a maximum PAH signal at $m/z = 276$.

Via the calibration discussed in section "Calibration" below the amount of OC as a function of d_m was quantitatively determined. These values (fg/particle) are shown in Figure 9. This figure is discussed in the next section.

Chemical Composition: Black Carbon

The AMS does not directly yield data on BC. However, as described in section "Estimate of Particle Mass, Density, and Dynamic Shape Factor" above, the BC content can be obtained via self-consistent mass balance calculations. In Figure 6 we show the best fit self-consistent values for the total particle mass and OC obtained by iterative solutions to the system of equations discussed in sections "Definitions of Mobility and Vacuum Aerodynamic Diameters" and "Estimate of Particle Mass, Density, and Dynamic Shape Factor" above. The difference between these two lines is the estimated BC content of the particles.

As is evident from Figure 9, the fractional composition of BC for each soot type is unchanged across the full range of mobility diameters studied, and the fractional content of BC is significantly greater for type 1 soot. For a given d_m, the estimated total mass is larger for type 2 soot. The ratio of m_p(type 1)/m_p(type 2) is 1.5 at $d_m = 100$ and increases to 7.5 at $d_m = 400$ nm.

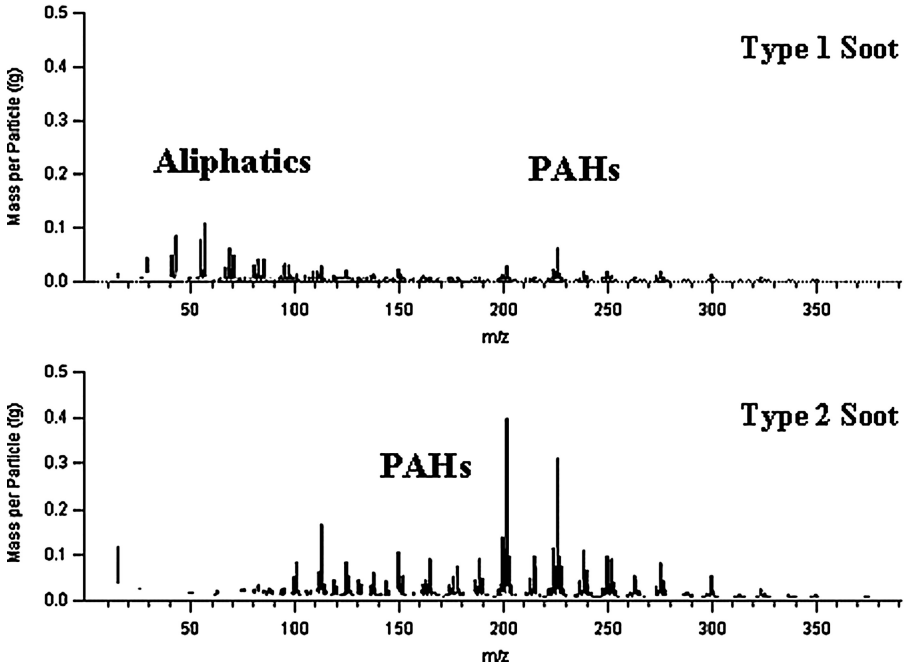

Figure 8. Mass spectra of type 1 and 2 soot ($d_m = 350$ nm). Note the difference in magnitude of the OC in the mass spectra.

As shown in the companion article (DeCarlo et al. 2004) and summarized in section "Further Comments on Estimating Particle Mass" above, the total particle mass (m_p) can also be estimated solely from the measurements of d_{va} and d_m. For the type 1 soot ($\phi = 2.5$) shown in Figure 9, the method of DeCarlo et al. (2004) yields an effective density of 0.25–1.00 g/cm^3, decreasing with d_m. The DeCarlo et al. (2004) method overpredicts the mass by 5–50%, increasing with d_m. For the type 2 soot ($\phi = 5.0$), an effective density of 1.3 g/cm^3 is obtained for the full range of d_m studied. For this soot the method of DeCarlo et al. (2004) overpredicts m_p by 1–10%, increasing with d_m.

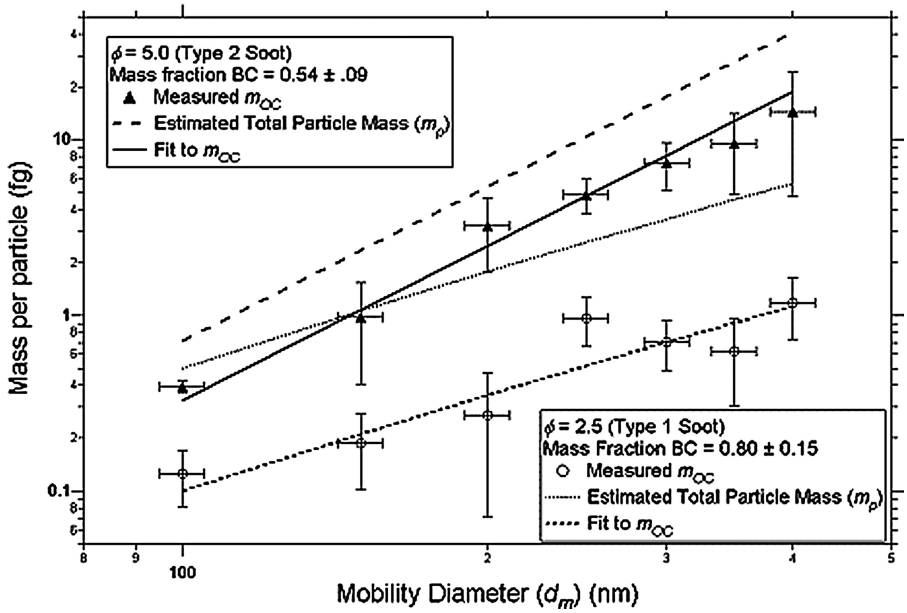

Figure 9. Mass per particle as a function of mobility diameter. Crosses denote experimental measurements of the OC mass per particle. Dotted and solid lines represent the best-fit self-consistent values obtained for total particle mass and OC component, respectively. The difference between the dotted and solid lines is the BC content.

Chemical Composition as a Function of Equivalence Ratio

The data in Figure 9 were obtained at two equivalence ratios: $\phi = 2.5$ (type 1 soot) and $\phi = 5.0$ (type 2 soot). Similar measurements were performed over the full range of ϕ studied (1.85–6.25). From these studies the fractional composition (mass fraction of BC, PAH, and aliphatic hydrocarbons) was determined as a function of ϕ and is shown in Figure 5. The error bars for the experimental points in Figure 5 have been omitted to simplify the figure. They are typically about ± 0.10 for type 1 soot and about ± 0.15 for type 2 soot.

As stated in connection with the vacuum aerodynamic diameter (see Figure 4), the transition between the two types of soot is sharp. This is also evident from the chemical composition (see Figure 5). For type 1 soot, the fractional composition of PAH and BC depends significantly on the equivalence ratio. At an equivalence ratio of 1.85, the BC mass fraction is 0.90, while the PAH mass fraction is about 0.05. As the equivalence ratio increases to 4.0, the BC mass fraction decreases to 0.75, while the PAH mass fraction increases to 0.20. The mass fraction of the aliphatic hydrocarbons is constant at about 0.05 for this range of equivalence ratios. For type 2 soot, however, the composition does not show a clear trend and within experimental accuracy is independent of equivalence ratio. Here the composition is approximately 0.50 PAH, 0.45 BC, and 0.05 aliphatic hydrocarbons. The fractional composition is independent of d_m for both types of soot.

As shown in Equation (10), the particle density can be determined from the composition with the assumption of no internal voids. For type 1 soot, as the equivalence ratio increases from 1.85 to 4.0, the density decreases from 1.80 to 1.55 g/cm^3. For type 2 soot, the density is 1.50 g/cm^3 independent of the equivalence ratio.

In Figure 6 the total particle mass of a $d_m = 350$ nm soot particle as a function of equivalence ratio is shown. The figure also shows the estimated fractal dimension, D_f, which is discussed in section "Fractal Dimension" below. The particle mass of type 1 soot exhibits significant dependence on ϕ. At $\phi = 1.85$, a 350 nm type 1 soot particle has a mass of about 3 fg. As ϕ increases to 4.0, the particle mass increases to 5 fg. However, for type 2 soot, the particle mass is relatively independent of equivalence ratio, with a 350 nm aerosol having a mass of about 25 fg. As will be discussed (see section "Discussion" below), the data in Figures 5 and 6 support a formation mechanism of type 1 and type 2 soot.

Dynamic Shape Factor

Further information about the soot particles may be obtained from the dynamic shape factor (χ). The parameter χ is determined by the iterative procedure described in section "Estimate of Particle Mass, Density, and Dynamic Shape Factor" (with the assumption $\chi = \chi_t = \chi_v$. In Figure 7 we show χ as a function of equivalence ratio (ϕ) for $d_m = 150$ nm and 350 nm. As ϕ increases from 1.85 to 4.0 (type 1 soot), χ decreases. Over this range of ϕ, χ also increases with increasing d_m. At $\phi > 4.0$ (type 2 soot), χ is constant at 1.1 ± 0.1 for the full range of d_m studied.

To frame the above observations, we note that for a sphere $\chi = 1$. For a cylinder with an axial ratio of 4 (length/diameter), $\chi = 1.2$; for an axial ratio of 10, $\chi = 1.4$. For a compact cluster of 4 spheres, $\chi = 1.2$ (Hinds 1999).

A value of $\chi = 1.1$ for type 2 soot implies a compact, nearly spherical shape that remains constant with d_m. On the other hand, the larger values of χ for type 1 soot imply a shape that deviates significantly from a sphere and the deviation increases with increasing d_m. As will be discussed in section "Application of AMS Laboratory Studies to Field Observations," this type of behavior is consistent with the results of Park et al. (2004a, b).

Fractal Dimension

As described in the data analysis section, the estimated fractal dimension (D_f) is obtained from a plot of $\log(m_p)$ versus $\log(d_m)$ (see Equation (15)). This plot is shown in Figure 9 for equivalence ratios (ϕ) of 2.5 (type 1 soot) and 5.0 (type 2 soot). The slope of this plot is D_f and the intercept is $\log(C')$. From the slopes in Figure 9 we obtain $D_f = 1.7 \pm 0.15$ for an equivalence ratio of 2.0 and $D_f = 2.95 \pm 0.10$ for $\phi = 5.0$ (within experimental error the total mass m_p and BC mass m_{BC} have the same dependence on d_m).

The analysis displayed in Figure 9 was repeated for the entire range of ϕ studied. As is shown in Figure 6, the estimated fractal dimension is unaffected by ϕ for a particular soot type, and there is a sharp transition in the value of D_f from $D_f = 1.7 \pm 0.15$ (type 1 soot) to $D_f = 2.95 \pm 0.10$ (type 2 soot) at $\phi = 4.0$. Note again that for a sphere, $D_f = 3$, and for an infinitely long linear aggregate, $D_f = 1$.

As discussed in section "Fractal Dimension of Soot" above, the value of D_f for type 1 soot is outside the limits in which the mass-mobility relationship (used to estimate D_f) is fully valid. It has not been verified how far into the transition regime the relationship is valid. This introduces additional uncertainty into our estimate of D_f. However, as is shown in sections "Discussion" and "Application of AMS Laboratory Studies to Field Observations" below the D_f estimated for type 1 soot is consistent with existing theoretical and experimental work.

DISCUSSION

In section "Introduction" above, we outlined the current model of soot formation. For convenience, we summarize the discussion here. Incomplete combustion of most fuels produces PAH compounds of various molecular weights that grow via reaction of small precursors such as acetylene radicals. The high temperatures within the flame cause most of the hydrogen atoms to be stripped from these structures, leaving BC. This process is most efficient at high temperatures, although under usual flame conditions some PAH molecules survive this process and do not form BC. The BC becomes a solid in the flame, at temperatures where the surviving PAHs are still in the vapor state. The BC

forms small spherules of about 15–30 nm in diameter (Palmer and Cullis 1965; Heywood 1988). These spherules coagulate to form fractal aggregates. As the particles move away from the hotter regions of the flame, the surviving PAHs (and aliphatic hydrocarbons) condense on the BC aggregates (see Glassman 1996).

It may be inferred from the soot formation model that the characteristics of the soot particles depend strongly on the flame temperature. Under the conditions of this study, the flame temperature is determined by the equivalence ratio (ϕ), with lower values of ϕ leading to higher flame temperatures. As discussed below, the results of our experiments agree qualitatively with the overall model of soot formation presented above. An estimate of the fractal dimension, dynamic shape factor, and the observation of the two types of soot produced provides additional information.

In accord with the above model, our results show that the soot particles formed at the higher temperatures (type 1 soot) are principally composed of BC (see Figure 5). The fractal dimension of type 1 soot is also consistent with the model. The BC spherules produced in the flame are expected to move randomly, colliding with each other to form agglomerates. The fractal dimension of such agglomerates is predicted by a mathematical simulation to be 1.8–1.95 (Meakin 1986). This is in good agreement with the value of 1.7 obtained in this study for type 1 soot (see Figure 6). This result for type 1 soot is also in agreement with light-scattering experiments on sooting in acetylene/air diffusion flames (Sorensen and Feke 1996).

As shown in Figure 5, for type 1 soot, the mass fraction of BC decreases and the mass fraction of PAH increases with increasing equivalence ratio (ϕ) (i.e., decreasing flame temperature). This is consistent with the expected higher concentration of PAH compounds surviving at lower flame temperatures and subsequently condensing on soot aerosols. In Figure 6, the increase in vacuum aerodynamic diameter (d_{va}) and mass of the type 1 soot particle with increasing ϕ is consistent with increasing condensation of PAHs.

As shown in Figure 7, the shape factor decreases with increasing equivalence ratio (ϕ) (decreasing flame temperature) in keeping with the expectation that the aerosol will become more spherical with increased condensation, although the fractal dimension does not change. Note that the dynamic shape factor and fractal dimension are connected to two different properties of the particle. The dynamic shape factor deals with increased drag on the particle due to nonspherical shape, while the fractal dimension deals with a reduction in mass due to nonspherical shape. A change in χ for constant D_f has been previously observed (e.g., Park et al. 2003, 2004a, b) and is predicted in the companion article (DeCarlo et al. 2004).

The sharp transition between type 1 and type 2 soot in aerosol composition (Figure 5), in mass-per-particle and fractal dimension (Figure 6), and in dynamic shape factor (Figure 7) is clear. While we cannot provide a definitive explanation for this sharp transition, the following hypothesis seems reasonable. As suggested above, condensation of PAH compounds on type 1 soot proceeds into the interior of the porous soot. As the equivalence ratio increases (flame temperature decreases), the PAH vapor concentration increases, and a point is reached where the pores and irregularities of the soot are filled by the condensed PAH compounds and the individual spherules lose their identity. This is the transition point where the particle becomes a nearly smooth sphere and the fractal dimension switches from 1.7 to 2.95 (3 for a sphere).

To explain the sharp increase in the particle mass at the transition point from type 1 soot to type 2 soot for a constant d_m (see Figure 6), we note that if an irregularly shaped particle of a given volume were converted to a smooth sphere, the mobility diameter would decrease (because χ decreases to 1; see Equation (4)). In Figure 8, we plotted the particle mass versus equivalence ratio for particles with $d_m = 350$ nm. Assuming that type 2 soot originated as type 1 soot, then before the soot became nearly spherical by condensation of PAH compounds, its mobility diameter was larger than 350 nm, and it contained more mass than a type 1 soot particle with $d_m = 350$ nm. A simple calculation based on the dependence of particle mass on d_m indicates that the almost spherical type 2 soot with $d_m = 350$ nm may have originated as a type 1 soot with $d_m = 650$ nm. Similar calculations can be performed for other values of d_m. The more detailed mechanism for such a fractal to near-spherical transformation is the subject of ongoing studies.

APPLICATION OF AMS LABORATORY STUDIES TO FIELD OBSERVATIONS

Data obtained in our laboratory studies can be used to help interpret some aspects of field measurements. For example, in AMS sampling plumes of diesel vehicles, Canagaratna et al. (2004) observed a small (80–100 nm) mode that is very similar to that in Figure 2 for the type 1 ($\phi < 4.0$) soot produced in the flame. In field studies in urban areas, the AMS instrument has identified two distinct particle modes appearing at different vacuum aerodynamic diameters ($d_{va} < 100$ nm and $d_{va} \sim 400$ nm) (see, for example, Allan et al. 2003b; Zhang et al. 2004b). In contrast, simultaneously measured mobility diameter mass distributions exhibited only a single mode centered at about 400 nm (Zhang et al. 2004b). Therefore, it appears that the 400 nm mobility diameter mode contains particles with both the smaller and larger vacuum aerodynamic diameters. Our laboratory results provide a possible explanation of this observed difference between the vacuum aerodynamic and mobility diameter size distributions. That is, the particles with $d_{va} < 100$ nm and no peak at a similar mobility diameter may be due to freshly emitted combustion-generated particles with a fractal character similar to our type 1 soot. The second mode, where the vacuum aerodynamic and mobility diameters are similar in distribution, suggest compact nonfractal particles. This interpretation is supported by analysis of wind patterns and sampling locations. The

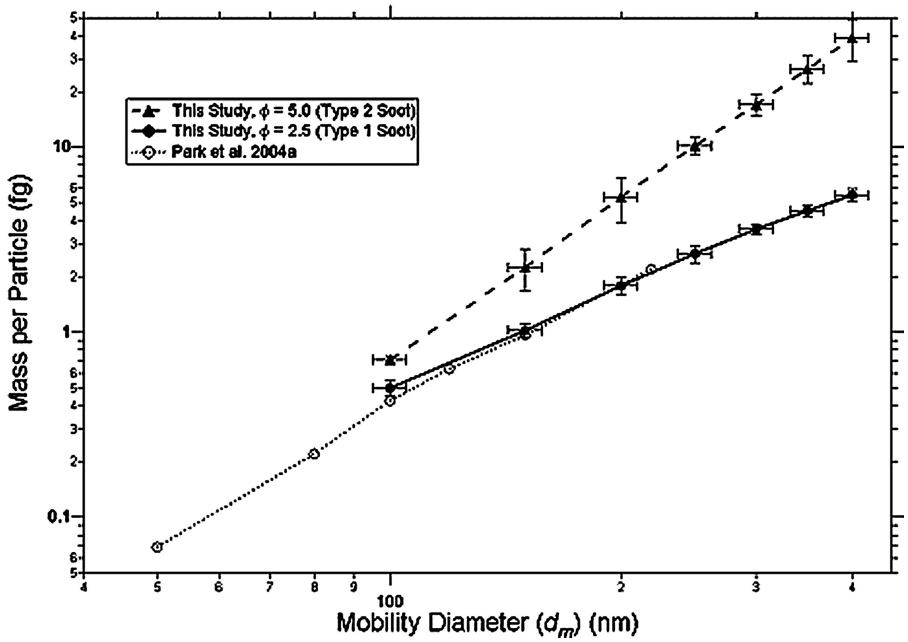

Figure 10. Particle mass as a function of mobility diameter for type 2 soot ($\phi = 5.0$), type 1 soot ($\phi = 2.5$), and diesel soot (Park et al. 2004a).

fractal-type particles correlate with urban locations, commuting hours, and combustion tracers (Zhang et al. 2004c; i.e., combustion sources), while the compact particles come from farther away and are aged. This is consistent with the interpretation of Zhang et al. (2004b) and with mass spectral analysis of the ambient and vehicle plume particles (Allan et al. 2003b; Canagaratna et al. 2004).

Park et al. (2003, 2004a, b) studied properties of soot emitted by diesel engines. Some of these properties are remarkably similar to those for the type 1 soot in this study, as illustrated in Figures 10 and 11. In Figure 10 we plot the particle mass versus the mobility diameter measured by Park et al. (2004a) (open circles) alongside of our results for type 1 and type 2 soot particles. In the region where the data overlap, the measurements of

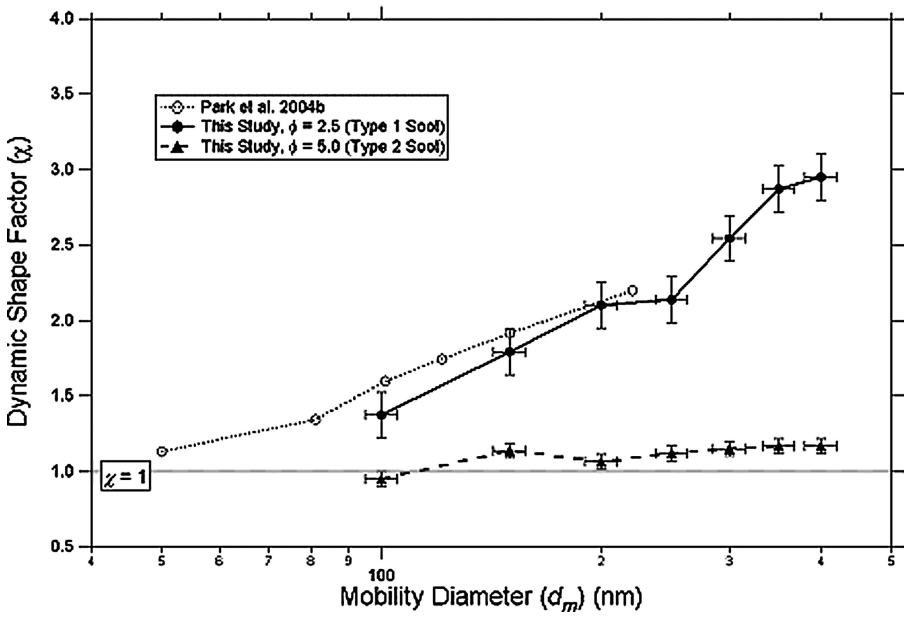

Figure 11. Dynamic shape factor (χ) as a function of mobility diameter for type 2 soot ($\phi = 5.0$), type 1 soot ($\phi = 2.5$), and diesel soot (Park et al. 2004a).

Park et al. (2004a) were similar to those for type 1 soot. Figure 11, in which the dynamic shape factor versus mobility diameter is plotted for the same three types of soot, also shows the similarity between type 1 soot and that observed by Park et al. (2004b). Van Gulijk et al. (2004) measured the mobility diameter and aerodynamic diameter of diesel soot particles under flow conditions where the aerodynamic diameter approaches d_{va} (see DeCarlo et al. 2004 for a detailed discussion of the effect of flow regimes on the aerodynamic diameter). Van Gulijk et al. (2004) observed that as d_m increased by 165 nm (from 115 to 280 nm), the aerodynamic diameter increased by only 24 nm (80 to 104 nm). This relationship is similar to type 1 soot.

While the relationship of dynamic shape factor, particle mass, and aerodynamic diameter to mobility diameter observed by Van Gulijk et al. (2004) and Park et al. (2003, 2004a, b) is similar to type 1 soot, the fractal dimension of soot reported by these authors is not the same as that measured in our study. Both authors reported a fractal dimension of about 2.4 for diesel soot, whereas the fractal dimension for type 1 soot measured in this study is 1.7 ± 0.15. The difference in fractal dimension between type 1 soot and the diesel soot studied by Park et al. (2003) may be understood in terms of the theory presented in Figure 9 of the companion article (DeCarlo et al. 2004). DeCarlo et al. show that the dynamic shape factor (which enters into fractal calculations) is formulated differently for fractal agglomerates with less than 60 primary particles ($d_m < 170$) than for larger agglomerates. DeCarlo et al. demonstrate that the fractal dimension for the smaller agglomerates is 2.46, and it transitions smoothly to 1.79 as the number of primary components in the agglomerate grows past 60 ($d_m > 170$ nm). This feature is evident in Figure 10. The slopes of the lines in that figure are the fractal dimensions. The difference in the slopes for the lower and higher d_m regions is clearly seen. The higher fractal dimension (2.4) for the Park et al. (2003) soot likely results from measurements being weighted toward lower d_m values.

REFERENCES

Albrecht, B. A. (1989). Aerosols, Cloud Microphysics, and Fractional Cloudiness, *Science* 245:1227–1230.

Allan, J. D., Jimenez, J. L., Coe, H., Bower, K. N., Williams, P. I., and Worsnop, D. R. (2003a). Quantitative Sampling Using an Aerodyne Aerosol Mass Spectrometer. Part 1: Techniques of Data Interpretation and Error Analysis, *J. Geophys. Res.—Atmos.* 108(D3):4090.

Allan, J. D., Coe, H., Bower, K. N., Williams, P. I., Gallagher, M. W., Alfarra, M. R., Jimenez, J. L., Worsnop, D. R., Jayne, J. T., Canagaratna, M. R., Nemitz, E., and McDonald, A. G. (2003b). Quantitative Sampling Using an Aerodyne Aerosol Mass Spectrometer. Part 2: Measurements of Fine Particulate Chemical Composition in Two UK Cities, *J. Geophys. Res.—Atmos.* 108(D3):4091.

Allen, M. D., and Raabe, O. G. (1982). Re-Evaluation of Millikan's Oil Drop Data for the Motion of Small Particles in Air, *J. Aerosol. Sci.* (6):537–547.

Allen, M. D., and Raabe, O. G. (1985). Slip Correction Measurements of Spherical Solid Aerosol Particles in an Improved Millikan Apparatus, *Aerosol Sci. Technol.* 4:269–286.

Bahreini R., Jimenez, J. L., Wang, J., Jayne, J. T., Worsnop, D. R., Flagan, R. C., and Seinfeld, J. H. (2003). Aircraft-Based Aerosol Size and Composition Measurements During ACE-Asia Using an Aerodyne Aerosol Mass Spectrometer, *J. Geophys. Res.—Atmos*. 108(D23):8645.

Baron, P. A., and Willeke, K. (2001). Gas and Particle Motion. In *Aerosol Measurement: Principles, Techniques, and Applications*, edited by P. A. Baron and K. Willeke. Wiley, New York, pp. 61–97.

Bockhorn, H. (ed.). (1994). *Soot Formation in Combustion: Mechanisms and Models of Soot Formation, Springer Series in Chemical Physics, Vol. 59*. Springer-Verlag, Berlin.

Canagaratna, M. R., Jayne, J. T., Ghertner, D. A., Herndon, S., Shi, Q., Jimenez, J. L., Silva, P. J., Williams, P., Lanni, T., Drewnick, F., Demerjian, K. L., Kolb, C. E., and Worsnop, D. R. (2004). Chase Studies of Particulate Emissions from in-use New York City Vehicles, *Aerosol Sci. Technol*. 38(6):555–573.

Choi, M. Y., Mulholland, G. W., Hamins, A. W., and Kashiwagi, T. (1993). Comparisons of Soot Volume Fraction Measurements Using Optical and Isokinetic Sampling Techniques, in *Chemical and Physical Processes of Combustion*, The Fall 1993 Meeting of the Eastern States Section of the Combustion Institute, Princeton, NJ, pp. 382–385.

Cruz, C. N., and Pandis, S. N. (1997). A Study of the Ability of Pure Secondary Organic Aerosol to Act as Cloud Condensation Nuclei, *Atmos. Environ.* 31:2205–2214.

DeCarlo, P., Worsnop, D. R., Slowik, J. G., Davidovits, P., and Jimenez, J. L. (2004). Particle Morphology and Density Characterization by Combined Mobility and Aerodynamic Diameter Measurements. Part 1: Theory, *Aerosol Sci. Technol.* 38(12):1185-1205.

Dobbins, R. A., Fletcher, R. A., and Chang, H. C. (1998). The Evolution of Soot Precursor Particles in a Diffusion Flame, *Combustion Flame* 115(3):285–298.

Flagan, R. C. (1999). On Differential Mobility Analyzer Resolution, *Aerosol Sci. Technol.* 30(6):556.

Frenklach, M., Clary, D. W., Gardiner, W. C. Jr., and Stein, S. E. (1984). Detailed Kinetic Modeling of Soot Formation in Shock Tube Pyrolysis of Acetylene. In *Twentieth Symposium (International) on Combustion*. The 1984 Meeting of The Combustion Institute, Pittsburgh, PA, pp. 887–901.

Glassman, I. (1996). *Combustion*, 3rd ed. Academic Press, San Diego, CA, pp. 399–430.

Gray, H. A., Cass, G. R., Huntzicker, J. J., Heyerdahl, E. H., and Rau, J. A. (1986). Characteristics of Atmospheric Organic and Elemental Carbon Particle Concentrations in Los Angeles, *Environ. Sci. Technol.* 20:580–589.

Hansen, J., and Nazarenko, L. (2004). Soot Climate Forcing via Snow and Ice Albedos, *Proc. Natl. Acad. Sci.* 101(2):423–428.

Haynes, B. S., and Wagner, H. G. (1981). Soot Formation, *Prog. Energy Combust. Sci.* 7(4):229–273.

Heberlein, J., Postell, O., Girshick, S., McMurry, P., Gerberich, W., Iordanoglu, D., Di Fonzo, F., Neumann, D., Gidwani, A., Fan, M., and Tymiak, N. (2001). Thermal Plasma Deposition of Nanophase Hard Coatings, *Surface Coatings Technol.* 142:256–261.

Heywood, J. (1988). *Fundamentals of Internal Combustion Engines*. McGraw-Hill, pp. 627–628.

Hinds, W. C. (1999). *Aerosol Technology*, 2nd ed. John Wiley & Sons, New York.

Huffman, J. A., Jayne, J. T., Onasch, T., Worsnop, D. R., and Jimenez, J. L. A Beam Width Probe for the Aerodyne Aerosol Mass Spectrometer, *Aerosol Sci. Technol.* submitted.

Jacobson, M. Z. (2001). Strong Radiative Heating Due to the Mixing State of Black Carbon in Atmospheric Aerosols, *Nature* 409:695–697.

Jayne, J. T., Leard, D. C., Zhang, X., Davidovits, P., Smith, K. A., Kolb, C. E., and Worsnop, D. R. (2000). Development of an Aerosol Mass Spectrometer for Size and Composition Analysis of Submicron Particles, *Aerosol Sci. Technol.* 33:49–70.

Jimenez, J. L., Bahreini, R., Cocker, D. R., III, Zhuang, H., Varutbangkul, V., Flagan, R. C., Seinfeld, J. H., O'Dowd, C. D., and Hoffman, T. (2003b). New Particle Formation from Photooxidation of Diiodomethane (CH_2I_2), *J. Geophys. Res.—Atmos.* 108(D10):AAC5/1-AAC5/25.

Jimenez, J. L., Bahreini, R., Cocker, D. R., III, Zhuang, H., Varutbangkul, V., Flagan, R. C., Seinfeld, J. H., O'Dowd, C. D., and Hoffman, T. (2003c). Correction to "New Particle Formation from Photooxidation of Diiodomethane (CH_2I_2)," *J. Geophys. Res.—Atmos.*108(D23):4733.

Jimenez, J. L., Jayne, J. T., Shi, Q., Kolb, C. E., Worsnop, D. R., Yourshaw, I., Seinfeld, J. H., Flagan, R. C., Zhang, X., Smith, K. A., Morris, J., and

Davidovits, P. (2003a). Ambient Aerosol Sampling with an Aerosol Mass Spectrometer, *J. Geophys. Res.—Atmos.* 108(D7):8425.

Kane, D. B., and Johnston, M. V. (2000). Size and Composition Biases on the Detection of Individual Ultrafine Particles by Aerosol Mass Spectrometry, *Envi. Sci. Technol.* 34(23):4887–4893.

Koren, I., Kaufman, Y. J., Remer, L. A., and Martins, J. V. (2004). Measurement of the Effect of Amazon Smoke on Inhibition of Cloud Formation, *Science.* 303:1342–1345.

Larson, S. M., Cass, G. R., and Gray, H. A. (1989). Characteristics of Summer Midday Low Visibility Events and the Los Angeles Basin, *Envir. Sci. Technol.* 10:118–130.

Lelieveld, J., Crutzen, P. J., Ramanathan, V., Andreae, M. O., Brenninkmeijer, C. A. M., Campos, T., Cass, G. R., Dickerson, R. R., Fischer, H., de Gouw, J. A., Hansel, A., Jefferson, A., Kley, D., de Laat, A. T. J., Lal, S., Lawrence, M. G., Lobert, J. M., Mayol-Bracero, O. L., Mitra, A. P., Novakov, T., Oltmans, S. J., Prather, K. A., Reiner, T., Rodhe, H., Scheeren, H. A., Sikka, D., and Williams, J. (2001). The Indian Ocean Experiment: Widespread Air Pollution from South and Southeast Asia, *Science* 291:1031–1036.

Lide, D. R. (ed.). (1992). *CRC Handbook of Chemistry and Physics.* CRC Press: Ann Arbor, MI.

Liu, P., Ziemann, P. J., Kittelson, D. B., and McMurry, P. H. (1995a). Generating Particle Beams of Controlled Dimensions and Divergence. I. Theory of Particle Motion in Aerodynamic Lenses and Nozzle Expansions, *Aerosol Sci. Technol.* 22(3):293–313.

Liu, P., Ziemann, P. J., Kittelson, D. B., and McMurry, P. H. (1995b). Generating Particle Beams of Controlled Dimensions and Divergence. II. Experimental Evaluation of Particle Motion in Aerodynamic Lenses and Nozzle Expansions, *Aerosol Sci. Technol.* 22(3):314–324.

McMurry, P. H., Wang, X., Park, K., and Ehara, K. (2002). The Relationship Between Mass and Mobility for Atmospheric Particles: A New Technique for Measuring Particle Density. *Aerosol Sci. Technol.* 36(2):227–238.

Meakin, P. (1986). *On Growth and Form*. Martinus Nijhoff, Dordrecht, The Netherlands.

Menon, S., Hansen, J., Nazarenko, L., and Luo, Y. (2002). Climate Effects of Black Carbon Aerosols in China and India, *Science* 297:2250–2253.

Milliken, R. C. (1962). Non-Equilibrium Soot Formation in Premixed Flames, *J. Phys. Chem.* 66:794.

Novakov, T., and Penner, J. E. (1993). Large Contribution of Organic Aerosols to Cloud-Condensation-Nuclei, *Nature* 365:823–826, 577–583.

Palmer, H. B., and Cullis, H. F. (1965). *The Chemistry and Physics of Carbon*, Vol. 1, Dekker, New York.

Pandis, S. N., Wexler, A. S., and Seinfeld, J. H. (1995). Dynamics of Tropospheric Aerosols, *J. Phys. Chem.* 99:9646–9659.

Park, K., Cao, F., Kittelson, D. B., and McMurry, P. H. (2003). Relationship Between Particle Mass and Mobility for Diesel Exhaust Particles, *Environ. Sci. Technol.* 37:577–583.

Park, K., Kittelson, D. B., and McMurry, P. H. (2004b). Structural Properties of Diesel Exhaust Particles Measured by Transmission Electron Microscopy (TEM): Relationships to Particle Mass and Mobility, *Aerosol Sci. Technol.* 38(9):881–889.

Park, K., Kittelson, D. B., Zachariah, M. R., and McMurry, P. H. (2004a). Measurement of Inherent Material Density of Nanoparticle Agglomerates, *J. Nanoparticle Res.* 6(2–3):267–272.

Posfai, M., Anderson, J. R., and Buseck, P. R. (1999). Soot and Sulfate Aerosol Particles in the Remote Marine Troposphere, *J. Geophys. Res.* 104(D17):21,685–21,693.

Ramanathan, V., Cruzen, P. J., Kiehl, J. T., and Rosenfeld, D. (2001). Aerosols, Climate, and the Hydrologic Cycle, *Science* 294:2119–2124.

Sato, M., Hansen, J., Koch, D., Lacis, A., Ruedy, R., Dubovik, O., Holben, B., Chin, M., and Novakov, T. (2003). Global Atmospheric Black Carbon Inferred from AERONET, *Proc. Natl. Acad. Sci., USA* 100:6319–6324.

Schug, K. P., Manheimer-Timnat, Y., Yaccarino, P., and Glassman, I. (1980). Sooting Behavior of Gaseous Diffusion Flames and the Influence of Additives, *Combust. Sci. Technol.* 22:235.

Schmidt-Ott, A., Baltensperger, U., Gaggeler, H. W., and Jost, D. T. (1990). Scaling Behavior of Physical Parameters Describing Agglomerates, *J. Aerosol Sci.* 21(6):711–717.

Smith, O.I. (1981). Fundamentals of Soot Formation in Flames with Application to Diesel Engine Particulate Emissions, *Prog. Energy Combust. Sci.* 7(4):275–291.

Sorensen, C. M., and Feke, G. D. (1996). The Morphology of Macroscopic Soot, *Aerosol Sci. Technol.* 25(3):328–337.

Tobias, H. J., Kooiman, P. M., Docherty, K. S., and Ziemann, P. J. (2000). Real-time Chemical Analysis of Organic Aerosols Using a Thermal Desorption Particle Beam Mass Spectrometer, *Aerosol Sci. Technol.* 33(1–2):170–190.

Twomey, S. A., Peipgrass, M., and Wolfe, T. (1984). An Assessment of the Impact of Pollution on the Global Albedo, *Tellus*. 36B:356–366.

Van Gulijk, C., Marijnissen, J. C. M., Makkee, M., Moulijn, J. A., and Schmidt-Ott, A. (2004). Measuring Diesel Soot with a Scanning Mobility Particle Sizer and an Electrical Low-Pressure Impactor: Peformance Assessment with a Model for Fractal-like Aggregates, *J. Aerosol. Sci.* 35:633–655.

Zhang, Q., Alfarra, M. R., Worsnop, D. R., Allan, J. D., Coe, H., Canagaratna, M. R., and Jimenez, J. L. (2004c). Deconvolution and Quantification of Primary and Oxygenated Organic Aerosols Based on Aerosol Mass Spectrometry. Part 1: Development and Validation of the Method, *Environ. Sci. Technol.* submitted.

Zhang, Q., Canagaratna, M. R., Jayne, J. T., Worsnop, D. R., and Jimenez, J. L. (2004b). Time and Size-Resolved Chemical Composition of Submicron Particles in Pittsburgh—Implications for Aerosol Sources and Processes, *J. Geophys. Res.—Atmos*. in press.

Zhang, X., Smith, K. A., Worsnop, D. R., Jimenez, J., Jayne, J. T., and Kolb, C. E. (2002). A Numerical Characterization of Particle Beam Collimation by an Aerodynamic Lens-Nozzle System. Part I: An Individual Lens or Nozzle, *Aerosol Sci. Technol.* 36(5):617–631.

Zhang, X., Smith, K. A., Worsnop, D. R., Jimenez, J. L., Jayne, J. T., Kolb, C. E., Morris, J., Davidovits, P. (2004a). Characterization of Particle Beam Collimation: Part II Integrated Aerodynamic Lens-Nozzle System, *Aerosol Sci. Technol.* 38(6):619–638.

APPENDIX A. LIST OF SYMBOLS

C	constant relating R_g and D_f
C'	constant relating d_m and D_f
C_c	cunningham slip correction
D_f	fractal dimension
d_{ve}	volume equivalent diameter
d_m	mobility diameter
d_{pp}	diameter of primary particle in agglomerate
d_{va}	vacuum aerodynamic diameter
F_D	drag force on a particle
k_1	proportionality constant between R_g and d_m
m_{AL}	aliphatic mass per particle
m_{BC}	BC mass per particle
m_p	particle mass
m_{PAH}	PAH mass per particle
N_{pp}	number of primary particles in an agglomerate
R_g	radius of gyration
RIE	relative ionization efficiency
V	particle velocity
V_p	particle volume
χ	dynamic shape factor (any regime)
χ_t	dynamic shape factor (transition regime)
χ_v	dynamic shape factor (free-molecular regime)
Ø	fuel equivalence ratio
η	gas viscosity
λ	mean free path
ρ_0	unit density (1 g/cm^3)

ρ_{AL} density of aliphatics
ρ_{BC} density of BC
ρ_p particle density
ρ_{PAH} density of PAHs

APPENDIX B

As discussed in the text, with the assumption $\chi = \chi_t = \chi_v$, the following relationship is obtained from Equations (4) and (6):

$$\frac{\rho_p \cdot d_{ve}^2}{C_c(d_{ve})} = \frac{d_m \cdot d_{va} \cdot \rho_o}{C_c(d_m)}. \quad [B1]$$

Note the right-hand side term is experimentally determined. This equation cannot be solved algebraically for d_{ve} because of the type of functional dependence of $C_c(d_{ve})$ on d_{ve}. However, a simple solution for d_{ve} may be obtained when d_e is either very small or very large with respect to the molecular mean free path (λ). For small d_{ve}, $C_c(d_{ve})$ may be expanded (from Equation (5)) as

$$C_c(d_{ve}) = 1 + \frac{\lambda}{d_{ve}}\left[2.34 + 1.05\left(1 - 0.39\frac{d_{ve}}{\lambda} + \cdots\right)\right]. \quad [B2]$$

In the limit of small d_{ve}, Equation (B1) may be expressed as

$$C_c(d_{ve}) \approx 3.39\frac{\lambda}{d_{ve}} \quad (d_{ve} \ll \lambda). \quad [B3]$$

Substituting this expression into Equation (B1) yields

$$d_{ve}^3 \rho_p = \frac{3.39\rho_0 \cdot d_m \cdot d_{va}}{C_c(d_m)}. \quad [B4]$$

As is evident from Equation (B4), when $d_{ve} \ll \lambda$, m_p is fully determined simply by the measurement of d_m and d_{va} independent of knowledge of the particle density. In this case, $dm_p/m_p = 0$.

In the limit of large d_{ve} ($d_{ve} \gg \lambda$), $C_c(d_{ve}) = 1$. Substituting this value into Equation (B1) and solving for d_{ve} yields

$$d_{ve} = \left(\frac{d_{va} \cdot d_m \cdot \rho_0}{\rho_p \cdot C_c(d_{ve})}\right)^{1/2}. \quad [B5]$$

From Equations (7) and (B5), the particle mass can be expressed as:

$$m_p = \frac{\pi}{6}\left(\frac{d_{va} \cdot d_m \cdot \rho_0}{C_c(d_e)}\right)^{3/2} \cdot \rho_p^{-1/2} \quad [B6]$$

Differentiating Equation (B6) and normalizing the result to m_p yields $\frac{dm_p}{m_p} = -\frac{1}{2}\frac{d\rho_p}{\rho_p}$. Between these two limiting cases the relationship between dm_p/m_p and $d\rho_p/\rho_p$ is obtained by a numerical solution to Equation (B1).

In solving Equation (B1), we assume some reasonable value of ρ_p. The d_{ve} is then obtained for the values $(\rho_p + \Delta\rho_p)$. The particle mass is given by Equation (7), yielding the value of Δm_p for a given ρ_p. These results are displayed in Figure B1, which is a plot of $\Delta m_p/m_p$ versus $\Delta\rho_p/\rho_p$ for a few of the combinations of d_{va} and d_m observed in this study. In this figure, the $\Delta m_p/m_p$ values are calculated with respect to an assumed density of 1.5 g/cm^3. The d_{ve} values in the box insert are obtained via Equation (2). The calculations in Figure B1 can be generalized to any combination of d_m and d_{va} by noting that, for a given ρ_p, any d_m and d_{va} that yield (via Equation (B1)) the same d_{ve} will result in the same relationship between $\Delta m_p/m_p$ and $\Delta\rho_p/\rho_p$.

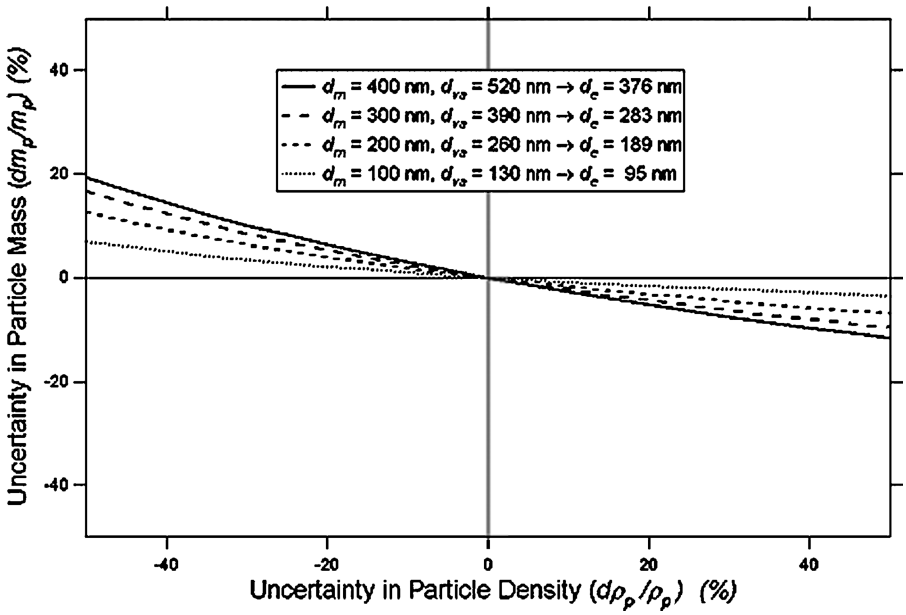

Figure B1. Uncertainty in particle mass versus uncertainty in particle density. The quantity $d\rho_p/\rho_p$ is expanded about a density of 1.5 g/cm^3. Uncertainties are expressed as a percentage of particle mass (assuming $\rho_p = 1.5$ g/cm^3).